



HAL
open science

Comparison of the experimental response of two horizontal axis tidal turbines to wave and current

Marc-amaury Dufour, Benoît Gaurier, Grégory Pinon, Grégory Germain, Jean-Valéry Facq, Michael Togneri, Fabio Represas, Erwann Nicolas, Julie Marcille

► To cite this version:

Marc-amaury Dufour, Benoît Gaurier, Grégory Pinon, Grégory Germain, Jean-Valéry Facq, et al.. Comparison of the experimental response of two horizontal axis tidal turbines to wave and current. 25ème Congrès Français de Mécanique - CFM 2022, Aug 2022, Nantes, France. hal-03938650

HAL Id: hal-03938650

<https://normandie-univ.hal.science/hal-03938650>

Submitted on 13 Jan 2023

HAL is a multi-disciplinary open access archive for the deposit and dissemination of scientific research documents, whether they are published or not. The documents may come from teaching and research institutions in France or abroad, or from public or private research centers.

L'archive ouverte pluridisciplinaire **HAL**, est destinée au dépôt et à la diffusion de documents scientifiques de niveau recherche, publiés ou non, émanant des établissements d'enseignement et de recherche français ou étrangers, des laboratoires publics ou privés.

Comparison of the experimental response of two horizontal axis tidal turbines to wave and current

Marc-Amaury Dufour^a, Benoît Gaurier^b, Grégory Pinon^{a,*}, Grégory Germain^b, Jean-Valéry Facq^b, Michael Togneri^c, Fabio Represas^d, Erwann Nicolas^e, Julie Marcille^e

a. LOMC, Normandie Univ, UNILEHAVRE, UMR 6294 CNRS, 76600 Le Havre, France

b. IFREMER, 150 quai Gambetta, BP 699, 62321 Boulogne-sur-mer, France

c. Energy & Environment Research Group, Swansea University, Bay Campus, Swansea SA1 8EN, UK

d. Magallanes Renovables, Prego de Montaos 7, Redondela, 36800, Spain

e. Sabella S.A., 7 Rue Felix Le Dantec, 29000 Quimper, France

Résumé :

Dans ce papier est étudiée expérimentalement l'influence de la houle et du courant combinés sur le comportement de deux hydroliennes à axe horizontal pré-commerciales. Les essais sont réalisés dans un bassin à houle et courant où les conditions d'essais sont obtenues par vélocimétrie laser. La vitesse moyenne de l'écoulement est calculée par intégration sur le disque rotor. Les amplitudes de houle et les orbitales de vague sont déterminées par méthode des moindres carrés.

Une attention particulière est apportée sur l'influence de la profondeur d'immersion des turbines. L'analyse des performances et des efforts sur les pales met en évidence une augmentation des fluctuations d'efforts avec la diminution de la profondeur.

Le moment de mise en rotation en pied de pale sur une turbine subit des fluctuations allant jusqu'à 100 % de l'effort moyen sous l'effet de la houle et de la turbulence lorsque la turbine est proche de la surface libre. La houle est responsable de la moitié de cette fluctuation.

Abstract:

This paper studies wave influence on two horizontal axis tidal turbines from industrial partners : Sabella and Magallanes. The trials have been performed in a wave and current flume tank where upstream flow conditions have been monitored thanks to Laser Doppler Velocimetry. Mean velocity is computed with rotor disc integration of the velocity profile. Wave amplitude and orbital amplitude are computed thanks to least mean square method.

A special attention has been paid to turbine immersion depth. Performance and blade root loads analysis highlight higher fluctuations when the turbine is close to the free surface.

When a turbine is close to the free surface, the edgewise moment fluctuations can reach 100 % of the mean effort under combined wave and turbulence loading. Wave is responsible for half part of these fluctuations.

Key words: Horizontal axis tidal turbine, Tidal energy converters, Wave-current interaction, Blade root loads, Fluctuating loads

*. Corresponding author : gregory.pinon@univ-lehavre.fr

1 Introduction

Tidal Energy Converters (TEC) experience harsh conditions, including strong upstream flows such as the ones encountered in the Alderney Race. In this highly energetic area, the turbulence intensity is about 6 % to 13 % [14], and wave can reach a significant height of 7 m and a peak period of 13 s during the Eleanor storm [9] for instance.

The MONITOR project was launched in 2018 [15]. The main objective of this project is to improve the TEC reliability facing those severe real-life conditions. This program is supported by the Interreg Atlantic Area because the Atlantic region in western Europe presents one of the biggest tidal potential in the world. Through multiple testing techniques: in-situ measurements, numerical simulations, and flume tank trials, the MONITOR project aims at better understanding TEC response to such conditions.

Based upon former studies evaluating TEC blade loads variations due to turbulence [11, 1], experimental testings carried out during the MONITOR project enabled TEC response to turbulence [13] to be quantified. It is especially shown that loads standard deviation at peak performance Tip Speed Ratio, i.e. nominal TSR, are three times higher in high turbulence cases versus low turbulence cases. Moreover, depending on TEC design, turbulence may affect positively or negatively the overall turbine performance of a few percents.

The present work, as part of flume tank testings of the MONITOR project, investigates TEC response to combined wave and turbulence effects. Previous studies [3, 7] have investigated the TEC response to wave exposure. All studies agree that TEC torque and thrust standard deviation drastically increase in wave cases, with an amplitude depending on wave parameters, immersion of the turbine and TSR. Nevertheless, it is still unclear if the effect of waves combined with a high turbulence level environment can be compared to a turbulent flow only from a material constraints point of view. The aim of the present work is to quantify this combined effect in order to reproduce as much as possible the in-situ conditions and the corresponding blade root loads variations. This experimental study focuses on two pre-commercial devices from industrial partners of the MONITOR project. First, there is the Magallanes ATIR. A 2 MW device composed of a floating platform supporting two variable-pitch 3-bladed turbines. Secondly, there is the Sabella D12 bottom-mounted fixed-pitch and 5-bladed 1 MW device.

First, the experimental set-up and the upstream flow conditions will be analyzed thoroughly in section 2. Secondly, the effect of waves on both performances C_P , C_T and blade root loads will be discussed in section 3.

2 Experimental set-up and upstream flow conditions

The set-up description of this section is very close to the one offered in [13], the present paper is a continuation of this previous work.

2.1 Experimental configuration and turbine models description

The experiments were carried out in the IFREMER wave and current flume tank in Boulogne-sur-Mer. The flume tank working section is 18 m long, 4 m wide and $H = 2$ m deep. The streamwise flow velocity ranges from 0.1 to 2.2 m/s. More details are available in [4]. The experimental set-up, illustrated in fig. 1, was the same for both turbines. The hub of the scaled turbine is set at a depth of either -1.0 m or -0.6 m below the free surface. The flow conditions were monitored at the hub center axis, approximately two turbine diameters upstream of the turbine with a bi-dimensional Laser Doppler Velocimeter (LDV). More details about the flume tank and the instrumentation can be found in [4, 13]. Both the

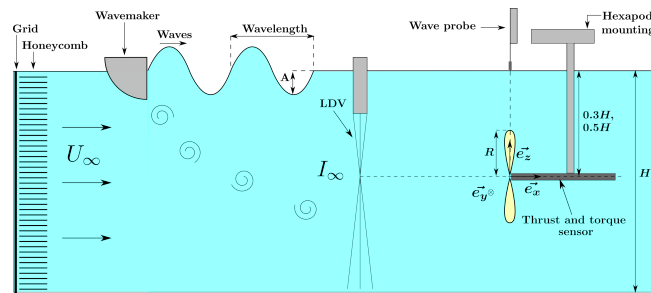


FIGURE 1 – Schematic side view of the test configuration with turbine immersion being either $0.3H$ or $0.5H$.

Magallanes Renovables ATIR and the Sabella D12 scaled models, shown in fig. 2, are based on the existing IFREMER mechanical and electrical generic turbine, a 3-bladed horizontal axis turbine, used in previous works [13, 5]. It is a fixed pitch device. This results in a major difference between the model and the full-scale device for the ATIR turbine. Whereas the full scale model has variable-pitch blades, the scaled model has fixed-pitch blades. Hence the ATIR blades will not be at the optimum pitch angle in all operating conditions. This is not an issue for the Sabella D12 turbine because full scale model is a fixed-pitch turbine. Model parameters are detailed in Table 1. Magallanes Renovables and Sabella blade profiles are confidential.

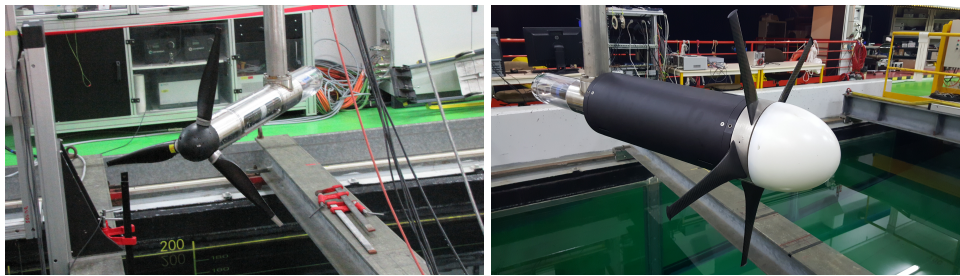


FIGURE 2 – Pictures of the scaled models: left is Magallanes Renovables' ATIR, right is Sabella's D12.

TABLE 1 – Turbine model parameter description.

Description	ATIR	D12
Rotor Radius R [mm]	338	300
Hub Radius [mm]	55	96
Number of blades	3	5

The scale of the ATIR and the D12 models are 1:28 and 1:20 respectively. The Froude criterion was preferred to the Reynolds criterion to scale the experimental set-up because the full scale Reynolds numbers are around 10^7 and these values cannot be obtained in the flume tank, as detailed in [13]. Be \bar{u} the velocity temporal mean, g the acceleration due to gravity and ν the water kinematic viscosity. Then the Froude number is $Fr = \bar{u}/(gH)$ and the Reynolds is $Re = \bar{u}R/\nu$. Under those definitions, the Froude equals to 0.18, for both real scale and experimental cases. The Reynolds number range in the flume tank, depending on the turbine, is $[2.4, 2.7] \times 10^5$.

In this study, the Tip Speed Ratio (TSR) varies from 0 to 8 for both turbine. The torque and thrust are directly measured on the rotation axis while each blade root is equipped with a load-cell measuring two

forces and three moments. These sensors and their axis system are represented on the rotor hub in fig. 3, see [4] for more details. These axis systems are the reference to name forces and moments of each blade root. Adapting the unconventional 5-bladed D12 to the IFREMER device forced to mount one blade

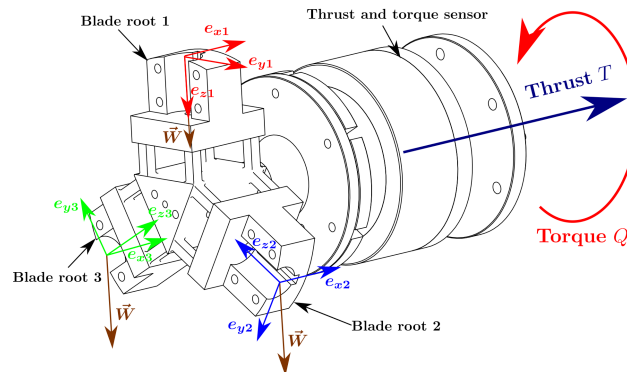


FIGURE 3 – Axis system for each blade root load and representation of weight \vec{W} for each blade. The weight is represented at the center of the axis system, and not at the gravity centre, to ease representation.

alone, and the four other blades by groups of two. Therefore, for the Sabella scaled turbine, the blade root loads can only be studied for the single blade.

Finally, during all the trials, the turbine parameters and the flow velocity are recorded synchronously. The signals are sampled at a frequency of 128 Hz, excepted for the LDV which has an irregular sampling rate. The acquisition time is set to 180 s for all cases.

Two cases are presented in this paper: "WM only" represents the case where the wavemaker is idle into the water, i.e. with current only. This case is mandatory to characterize the velocity profile and turbulence generated by the presence of the wavemaker. It is considered as the reference case. "A95-F05" represents the wave and current case, with a required wave amplitude of 95 mm (with no current) and wave frequency of 0.5 Hz.

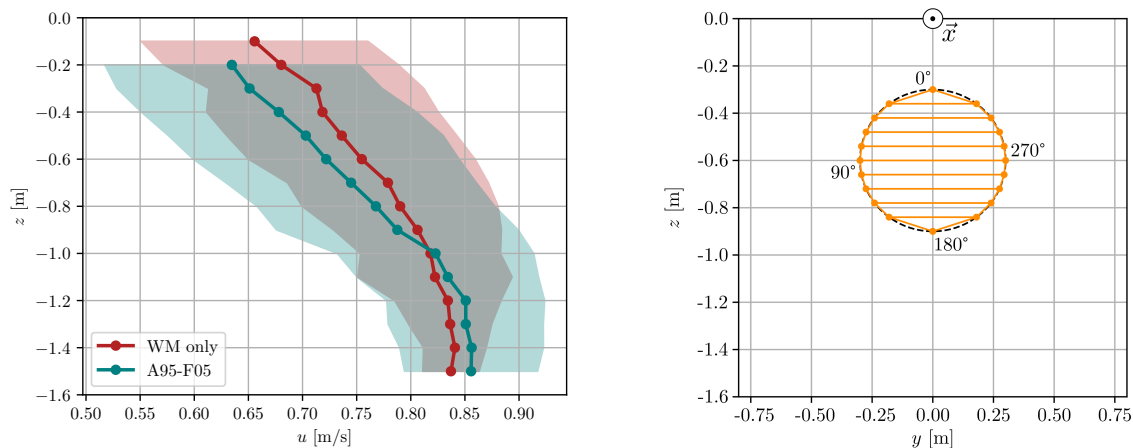
2.2 Upstream velocity conditions

The upstream velocity along x-axis at the hub center z-position is defined by eq.(1) in agreement with the axis system presented in fig. 1.

$$u(t) = \bar{u} + u'(t) + u_{wave}(t), \quad (1)$$

where \bar{u} is the temporal mean, $u'(t)$ is the fluctuating component due to turbulence and $u_{wave}(t)$ is the orbital velocity component along x-axis. If there are no wave, $u_{wave}(t) = 0$. The required mean upstream axial velocity in these trials is $u_0 = 0.80$ m/s. Specific mean upstream flow velocity will be found in Table 3.

Fig. 4a represents the velocity profile along the water column for the two tested cases. Dots on the velocity profiles represent mean values, noted $\bar{u}(z)$, linked by linear interpolation. The colored area represents the corresponding standard deviation. Concerning the profiles, the shear is linear between $z = -0.2$ m and $z = -1.0$ m for both cases. It can be noticed that "A95-F05" case has a shear with a higher slope. For $z < -1.0$ m, the velocity profile is nearly constant for both cases. An example of the position of the turbine rotor in the flume tank is shown in fig. 4b. The dashed lines stands for the turbine rotor disc for Sabella, $R = 300$ mm, at $z_0 = -0.6$ m. The rotor disc is seen from behind, facing upstream flow. To take into account the velocity variations along z , the velocity profiles are integrated on the rotor disc surface,



(a) Velocity profiles, mean \pm std, for "WM only" and "A95-F05" cases. (b) Disc integration scheme for Sabella D12, at depth -0.6 m.

FIGURE 4 – Velocity profiles processing.

as advised in [10]. Spatial integration through a trapezoidal approximation is used, as represented in fig. 4b by the orange polygones.

Moreover, several possible sources of error are identified. First these velocity profiles have been recorded with a tri-component LDV, different from the bi-component LDV used to record the velocity during the trials with the turbine model. This could lead to difference in the obtained velocity value. Secondly, these profiles were recorded at a different moment than the trials with the turbine model. As those trials are 180 s long, this could also lead to some convergence discrepancies. To avoid those errors, the integration is performed on velocity profiles normalized by the velocity mean at the hub z -position, z_0 .

This process results in coefficients named K_n , $n \in \{1, 2, 3\}$. They depend on the turbine type, the immersion depth and the time series. The time series can be $u(t)$, $u^2(t)$ or $u^3(t)$ and it gives the index of the coefficient. For all the cases, $K_1 \in [0.98, 1.00]$ serves to correct TSR , $K_2 \in [0.97, 1.00]$ serves to correct C_T , and $K_3 \in [0.96, 1.00]$ serves to correct C_P .

2.3 Turbulence

The incoming turbulence is at first regulated using flow straighteners, grid and honeycomb, placed at the inlet of the working section. Then the wavemaker presence generates turbulent structures that penetrate the water column. The ambient turbulence intensity in the flume tank is thus defined downstream of the wavemaker, at the bi-component LDV x -position, as presented in fig. 1.

The 3D turbulence intensity is defined by eq. (2). An isotropy assumption between the v and w components can be made. This signifies that for both of them, mean and standard deviation are of same order of magnitude. This hypothesis has been verified thanks to the velocity profile measurement with the tri-component LDV. The obtained I_{3D} at each depth highlights that the isotropy hypothesis between v and w components is valid for $z < -0.3$ m. Then, as the turbine hub is at $z_0 = -0.6$ m or $z_0 = -1.0$ m, this hypothesis is valid for the studied domain. This hypothesis allows to compute the 3D turbulence intensity with the data from the bi-component LDV by using the second measured velocity component twice. u , v , and w components are all decomposed in the same way as described in eq. (1). The turbulence intensity is computed with the contribution of turbulence only. That is to say the first order wave contribution, computed with an in-house sinusoidal least mean square code built according to [8], is subtracted from the velocity signal.

$$I_{3D} = \sqrt{\frac{1/3(\sigma_{u'}^2 + \sigma_{v'}^2 + \sigma_{w'}^2)}{\bar{u}^2 + \bar{v}^2 + \bar{w}^2}} \simeq \sqrt{\frac{1/3(\sigma_{u'}^2 + 2\sigma_{v'}^2)}{\bar{u}^2 + 2\bar{v}^2}} \simeq \sqrt{\frac{1/3(\sigma_{u'}^2 + 2\sigma_{w'}^2)}{\bar{u}^2 + 2\bar{w}^2}} \quad (2)$$

The wavemaker presence generates an ambient turbulence intensity around $I_{3D} \approx 10\%$ at -1.0 m to $I_{3D} \approx 15\%$ at -0.6 m. This turbulence intensity range corresponds to in-situ measured values [16, 9]. Specific turbulence intensity can be found for each case in Table 3.

2.4 Waves analysis

In this part, different approaches of processing the wave characteristics are investigated. The main objective here is to present the wave characteristics in the flume tank. A second objective is to highlight the possibility of rebuilding the wave orbital profiles under the free surface in further experimental analysis and in numerical works.

The measured wave amplitude comes from the wave probe signal processed with an in-house sinusoidal least mean square code built according to [8]. The wave orbital velocity along x-axis is defined by $u_{wave}(t) = b \sin(\omega_{wave}t) + c \cos(\omega_{wave}t)$ with $b, c \in \mathbb{R}$ also evaluated thanks to the same least mean square method. Then wave orbital amplitude equates $\sqrt{b^2 + c^2}$.

Airy's wave dispersion relation, from [12], is used to compute ideal wavenumber k_0 with an in-house built Newton procedure for equation resolution. Wave dispersion relation adapted to flume tank, i.e. with a current velocity, from [2], is solved with the same Newton's procedure for equation resolution. This gives a theoretical wavenumber for the flume tank k . From this, the wavelength L is obtained through $L = 2\pi/k$. Results are described in Table 2. For the "Theory" approach, the wave amplitude is computed with a formula from [2], characterizing the effect of the flume tank current on the wave amplitude. Results are in column "Wave "Theory" amplitude" of Table 2.

Eventually, two approaches are used to compute wave orbital amplitude. The first one is named "Theory" because it uses the previously obtained wave amplitude and the wavenumber k to compute orbital amplitude thanks to Airy's wave theory. The second one is named "Adjusted theory" because it uses the measured wave amplitude from the wave probe and the wavenumber k to compute orbital amplitude, again with Airy's wave theory.

Table 2 summarizes all the results obtained from this wave processing. The main objective of this pro-

TABLE 2 – Waves analysis.

Wave	f_{wave}	Theory wavelength L	Wave amplitude without current	Wave measured amplitude	Wave "Theory" amplitude	Depth	Orbital measured amplitude	Orbital "Theory" amplitude	Orbital "Adjusted theory" amplitude
-	Hz	m	mm	mm	mm	m	$m \cdot s^{-1}$	$m \cdot s^{-1}$	$m \cdot s^{-1}$
A95-F05	0.5	8.4	95	57	77	-1.0	0.08	0.10	0.07
						-0.6	0.11	0.13	0.10

cess is to characterize the wave of the upstream flow and showing that the "Adjusted theory" process is capable of producing accurate results on the wave orbital amplitude. This last point aims at proving the possibility of Airy's wave theory to reproduce accurately wave orbital amplitude measured in flume tank so that this process can be used to describe orbital through the water column in upcoming works.

The measured wave amplitude of 57 mm is significantly lowered compared to the required amplitude of 95 mm. A part of the explanation comes from the effect of the current in the flume tank, as highlighted in Table 2 with the "Wave "Theory" amplitude" column. However, this is not sufficient to account for all the decrease. The wavemaker transfer function must explain part of the gap between the "Theory" result

and the measurement. Moreover waves reflection in the flume tank as well as higher wave orders must have also played a role in the discrepancy between the "Theory" result and the measurement.

2.5 Summary of upstream flow conditions

In a word, major upstream flow parameters including mean velocity, turbulence intensity, measured wave amplitude, measured orbital amplitude, are summarized in Table 3.

TABLE 3 – Upstream flow major parameters.

Depth	Turbine	Wave	\bar{u}	I_{3D}	Wave measured amplitude	Orbital measured amplitude
m	-	-	$\text{m}\cdot\text{s}^{-1}$	%	mm	$\text{m}\cdot\text{s}^{-1}$
-1.0	ATIR	WM only	0.8	10.1	-	-
		A95-F05	0.81	10.8	57	0.08
	D12	WM only	0.79	9.3	-	-
		A95-F05	0.81	10.3	57	0.08
-0.6	ATIR	WM only	0.72	14.8	-	-
		A95-F05	0.7	15.7	57	0.11
	D12	WM only	0.72	15.4	-	-
		A95-F05	0.71	16.3	57	0.11

3 Turbines performances and blade root loads evaluation

Because of confidentiality aspects, values have to be normalized. The following reference case is used: "WM only" at -1.0 m depth at optimal performance TSR for each turbine: $TSR = 6.0$ for Magallanes and $TSR = 4.5$ for Sabella. For any load A , $\overline{A^{ref}}$ is the temporal average of this load for the reference case. Hence, normalized load $A^* = A/\overline{A^{ref}}$ is studied.

3.1 Power and thrust coefficients

Tip Speed Ratio is defined by:

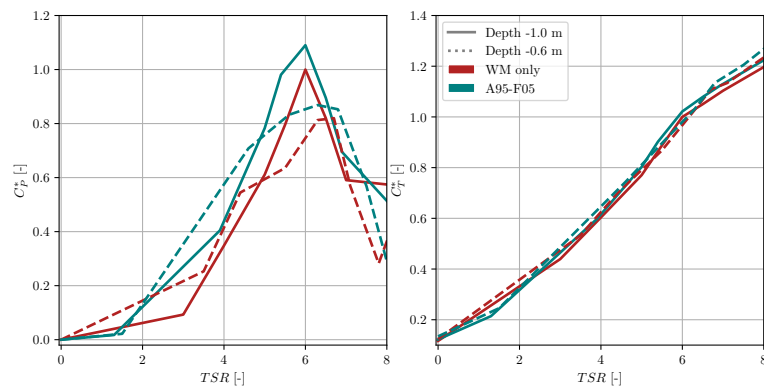
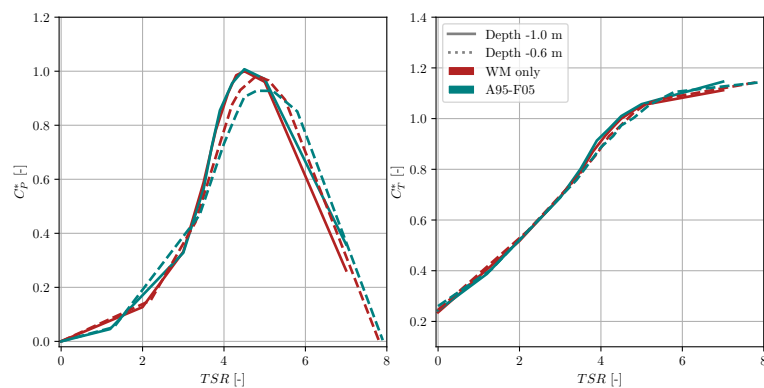
$$TSR = \frac{R\Omega}{K_1\bar{u}}, \quad (3)$$

where Ω is the turbine angular frequency. Power and thrust coefficient are defined by:

$$C_P = \frac{\bar{P}}{\frac{1}{2}\rho\pi R^2 K_3 \bar{u}^3} \quad C_T = \frac{\bar{T}}{\frac{1}{2}\rho\pi R^2 K_2 \bar{u}^2}, \quad (4)$$

where ρ is the fluid density. The power P and thrust T come from the torque and thrust sensor, see fig. 3. Fig. 5 presents C_P^* , C_T^* results versus TSR for Magallanes ATIR turbine, fig. 5a, and Sabella D12, fig. 5b. The C_T^* curves continuously increase with the TSR . Moreover, for one turbine, they are very close to each other whatever the case under investigation. The C_P^* curves are also common: increasing with the TSR , going through a maximum, then decreasing. An awaited result is the lower TSR of optimal performance of Sabella turbine compared to Magallanes one. This is explained by the higher solidity of Sabella turbine. Nevertheless, the curves present some discrepancies between the cases that deserve analysis.

As mentioned in [13], Magallanes Renovables ATIR turbine suffers from a strong Reynolds effect at $u_0 \simeq 0.8 \text{ m}\cdot\text{s}^{-1}$, partly because of the fixed-pitch model. Thus a possible way of explanation of the better C_P^* performance at both depth in the wave case "A95-F05" may be due to higher Reynolds encountered by the blades because of the orbital velocities. Nevertheless, comparison with [13] for this turbine can

(a) C_P^* and C_T^* for Magallanes ATIR turbine with $u_0 = 0.8$ m/s.(b) C_P^* and C_T^* for Sabella D12 turbine with $u_0 = 0.8$ m/s.FIGURE 5 – Performances of ATIR and D12 turbines versus TSR .

only be limited because the blades have a brand new rough coating. This coating deeply enhances the performances for the reference case "WM only" at -1.0 m depth compared to the equivalent case from [13]: high turbulence intensity at $u_0 \simeq 0.8 \text{ m}\cdot\text{s}^{-1}$. Finally the decrease in performance at -0.6 m may be due to the lower mean velocity at this depth. For the wave case "A95-F05", a decrease of 23 % of $C_{p,max}^*$ from -1.0 m depth to -0.6 m depth is observed. For the "WM only" case, a decrease of 19 % of $C_{p,max}^*$ from -1.0 m depth to -0.6 m depth is observed. Turbulence must not be responsible for this decrease because it has been shown in [13] that turbulence affects positively the performance of the Magallanes turbine. The shift of TSR at which occurs $C_{p,max}^*$: from $TSR = 6$ to $TSR = 6.5$ may be explained by higher turbulence as for Sabella turbine. But this effect was not observed in [13].

Concerning Sabella turbine analysis, it can be easily noticed that at -1.0 m depth, the wave doesn't affect the turbine performance: C_P^* curves are the same for both "WM only" and "A95-F05" cases. From -1.0 m depth to -0.6 m depth, for "WM only" case, the $C_{p,max}^*$ decreases of about 3 %. This effect is presented in [13] between the medium to high turbulence intensity cases. So this must confirm an effect of high turbulence intensity on Sabella turbine which slightly decreases the performances. Moreover, the TSR at which occurs $C_{p,max}^*$ is a little higher: $TSR = 4.5$ instead of $TSR = 4$, as seen in [13] and also observed for Magallanes turbine. From -1.0 m depth to -0.6 m depth, for "A95-F05" wave case, the $C_{p,max}^*$ decreases of about 9 %. This higher decrease in performance for this case may be due to the higher turbulence intensity at the -0.6 m depth and the stronger orbitals experienced. It may also be to the Reynolds effect as the mean velocity is lower at -0.6 m. The TSR at which occurs $C_{p,max}^*$ is even higher, nearly $TSR = 5$ instead of $TSR = 4$.

3.2 Blade root load analysis

Blade root loads indices are defined according to axis systems presented in fig. 3. Blade root loads are analyzed thanks to polar plots on fig. 6 for the edgewise moment M_{x1} and on fig. 7 for the thrust force F_{y1} . Angular phase of the blade root loads signal is built using Hilbert transform on F_{y1} , as already performed in [6]. The angular domain is then divided into sectors of angle θ_0 equating two times the angular resolution: $\theta_0 = 2\Omega/f_s$, where f_s is the sampling frequency. For each sector, if A is a blade root load, the normalized phase average is \widetilde{A}^* , and the normalized phase standard deviation is $\sigma_\theta^*(A)$. Only Magallanes results will be presented here because Sabella ones are still under processing.

3.2.1 M_{x1} processing and analysis

The angles are reported according to fig. 4b. h superscript is used here to denote the hydrodynamic component. As highlighted in fig. 3, weight affects the edgewise moment M_{x1}^* . In order to remove the effect of weight momentum M_P^* , the following data processing has been designed. The example taken here is for a turbine rotating in the counter clockwise, mathematically positive, direction of rotation according to fig. 4b. The edgewise moment can be divided between the hydrodynamic part and the weight part. We admit that the hydrodynamic momentum $\widetilde{M}_{x1}^{\theta,h}$ is equal at 90° and 270° because it is at the same water depth and thus the same averaged velocity. M_P^* is then obtained thanks to linear combination.

$$M_P^* = \frac{1}{2} \left(\widetilde{M}_{x1}^{\theta} (90^\circ) - \widetilde{M}_{x1}^{\theta} (270^\circ) \right) \quad (5)$$

Then, to isolate hydrodynamic effect, the projection of the weight momentum, as represented in fig. 3, is removed using eq. (5).

$$\widetilde{M}_{x1}^{\theta,h} = \widetilde{M}_{x1}^{\theta} - M_P^* \sin(\theta) \quad (6)$$

The result of this process is the polar representation of the hydrodynamic part of the edgewise moment, noted $\widetilde{M}_{x1}^{\theta,h}$. It is presented on fig. 6 polar plots. The striking element is the oval shape of $\widetilde{M}_{x1}^{\theta,h}$ for all cases and at both depth.

While $\min \widetilde{M}_{x1}^{\theta,h}$ is between 0° and 20° , $\max \widetilde{M}_{x1}^{\theta,h}$ is at 190° . This highlights a direction of asymmetry. It can also be observed with the gap between $\widetilde{M}_{x1}^{\theta,h}$ and \overline{M}_{x1}^* . $\widetilde{M}_{x1}^{\theta,h}$ is oval for both cases at both depth. This must result from the velocity gradient noticed on the profiles of fig. 4a. The angle of $\max \sigma_\theta^*(M_{x1})$ is close to the angle of $\max \widetilde{M}_{x1}^{\theta,h}$ at depth -0.6 m and it is close to the angle of $\min \widetilde{M}_{x1}^{\theta,h}$ at depth -1.0 m. There is a striking increase of \overline{M}_{x1}^* at -1.0 m for the wave case "A95-F05" which must explain the highest C_P^* previously observed in fig. 5a. At -0.6 m, \overline{M}_{x1}^* is also a little higher for "A95-F05" than for "WM only". However, this phenomenon is less important at -0.6 m than at -1.0 m.

TABLE 4 – Relative value of $\max \sigma_\theta^*(M_{x1})$

Depth	"WM only"	"A95-F05"
m	%	%
-0.6	80	100
-1.0	56	60

Table 4 shows the relative value of the maximum standard deviation of $\widetilde{M}_{x1}^{\theta,h}$. It represents a way to know the maximum amplitude of the fluctuating load encountered by the blade. Relative value of

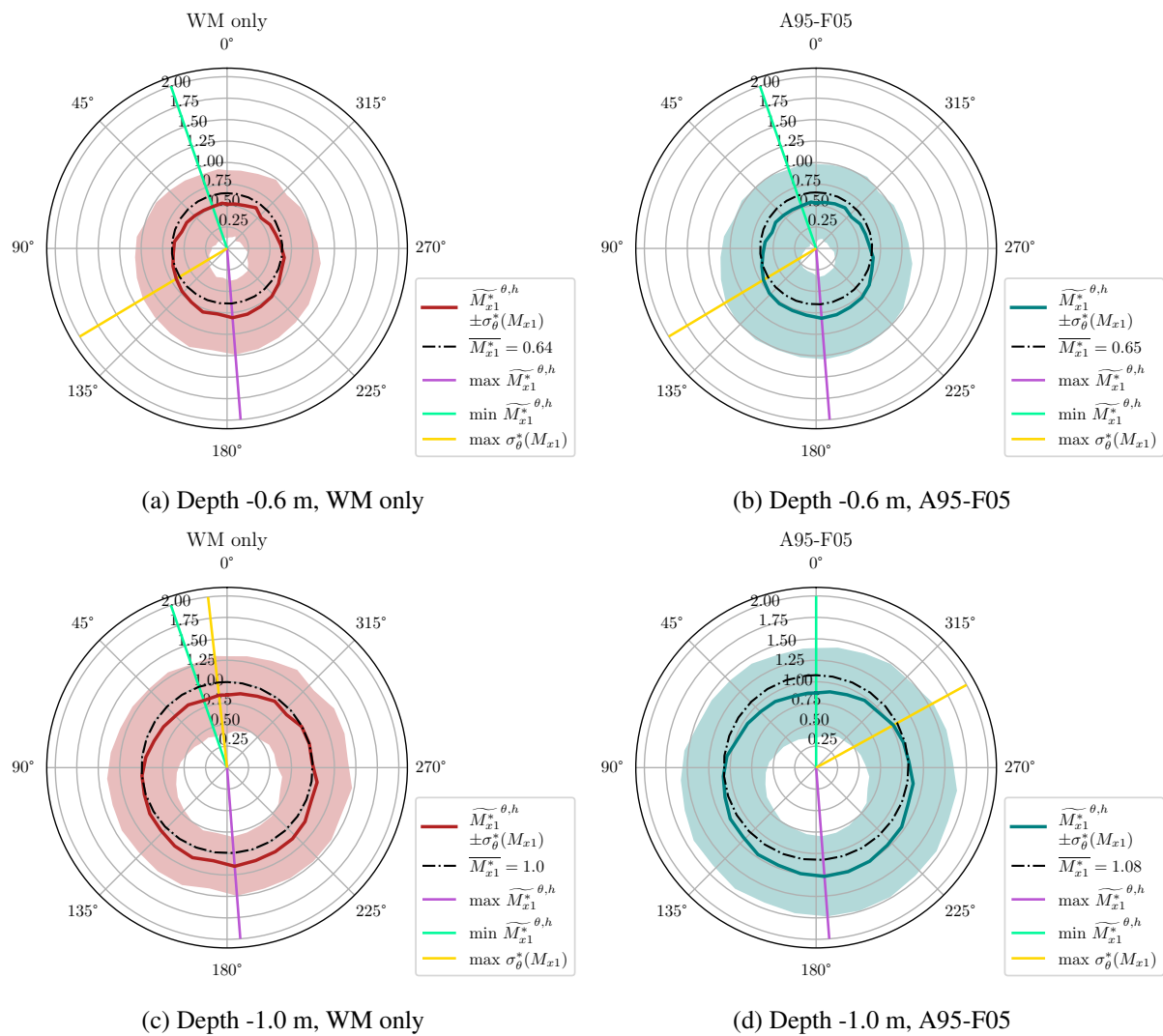


FIGURE 6 – $\widetilde{M}_{x1}^{*\theta,h}$ for Magallanes ATIR at peak performance $TSR = 6.7$ at depth -0.6 m and $TSR = 6.0$ at depth -1.0 m. The red data on the left represents the "WM only" case. The blue data on the right represents the "A95-F05" wave case. The red/blue line draws $\widetilde{M}_{x1}^{*\theta,h}$ for each angle. The red/blue area represents the standard deviation associated. Straight lines represent the direction of $\min \widetilde{M}_{x1}^{*\theta,h}$, green, $\max \widetilde{M}_{x1}^{*\theta,h}$, purple. Both represent the ovalized direction of the load. Eventually the yellow straight line represents the direction where the blade sees the higher load fluctuations: $\max \sigma_{\theta}^*(M_{x1})$.

$\max \sigma_{\theta}^*(M_{x1})$ is increasing when wave is added to turbulence ("A95-F05" case), and when the turbine gets closer to free surface from -1.0 m to -0.6 m. However, it is hard to determine the importance of variations only due to wave from Table 4 as the influences of turbulence and wave are mixed. To only measure the effects of wave, the amplitude of $\widetilde{M}_{x1}^{*\theta,h}$ variations have been processed using an in-house built sinusoidal least mean square method at the wave frequency [8]. At -1.0 m, the relative amplitude of this variations is 31 % of mean load value and at -0.6 m, it is about 46 % of mean load value. Hence those results highlight that wave seems to be responsible for half of the fluctuating loads represented in Table 4.

3.2.2 \widetilde{F}_{x1}^* analysis

Inasmuch as there is no effect of weight on F_{x1} , as it can be seen in fig. 3, the data can be directly plotted. \widetilde{F}_{x1}^* is represented on polar plot in fig. 7. The striking element is that the gap between \widetilde{F}_{x1}^* and \overline{F}_{x1}^* remains limited for all the angles. The standard deviation also appears limited compared to one encountered for the \widetilde{M}_{x1}^* signal.

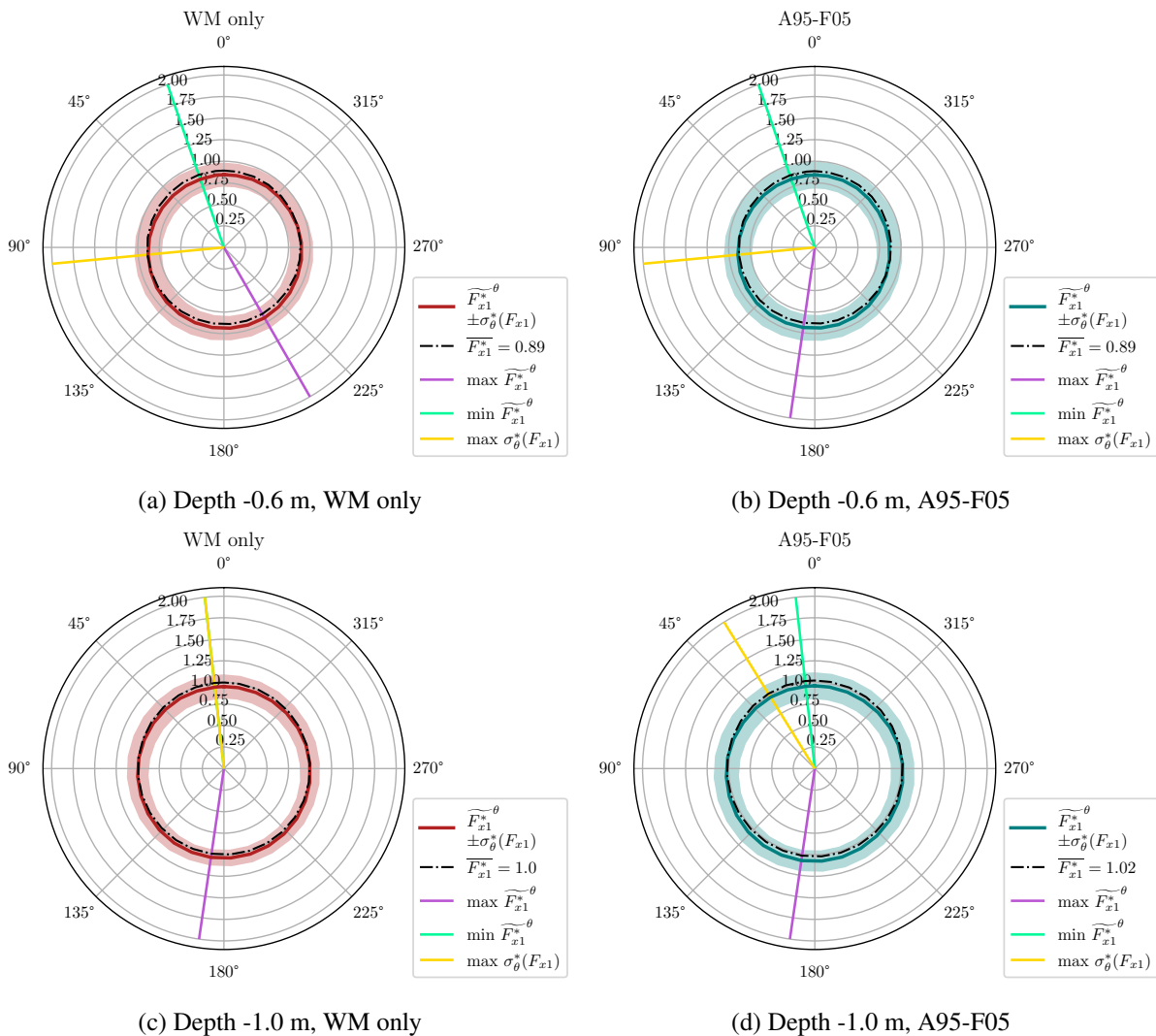


FIGURE 7 – \widetilde{F}_{x1}^* for Magallanes ATIR at peak performance $TSR = 6.7$ at depth -0.6 m and $TSR = 6.0$ at depth -1.0 m. The red data on the left represents the "WM only" case. The blue data on the right represents the "A95-F05" wave case. The red/blue line draws \widetilde{F}_{x1}^* for each angle. The red/blue area represents the standard deviation associated. Straight lines represent the direction of $\min \widetilde{F}_{x1}^*$, green, $\max \widetilde{F}_{x1}^*$, purple. Both represent the ovalized direction of the load. Eventually the yellow straight line represents the direction where the blade sees the higher load fluctuations: $\max \sigma_{\theta}^*(F_{x1})$.

While $\min \widetilde{F}_{x1}^*$ is at 0° for -1.0 m depth and at 20° for -0.6 m depth, $\max \widetilde{F}_{x1}^*$ is at 170° , excepted for "WM only" at -0.6 m case which is at 20° . The same direction of asymmetry as the one observed for \widetilde{M}_{x1}^* in section 3.2.1 is noticed. While $\max \sigma_{\theta}^*(F_{x1})$ is located between 5° and 30° at -1.0 m, it is located at 95° for -0.6 m cases. It is the same behaviour as the one observed for the \widetilde{M}_{x1}^* signal in

section 3.2.1. Thus $\max \sigma_{\theta}^*(F_{x1})$ and $\max \sigma_{\theta}^*(M_{x1})$ are apparently correlated.

Table 5 shows the relative value of the maximum standard deviation of $\widetilde{F_{x1}^*}^{\theta}$. It represents a way to know the maximum amplitude of the fluctuating loads encountered by the blade. $\max \sigma_{\theta}^*(F_{x1})$, which is about 16 % of mean load $\overline{F_{x1}^*}$ for all cases at both depth, seems less sensitive to wave or turbulence compared to $\max \sigma_{\theta}^*(M_{x1})$ reaching 100 % of mean effort in case of wave and turbulence at -0.6 m.

TABLE 5 – Relative value of $\max \sigma_{\theta}^*(F_{x1})$

Depth	"WM only"	"A95-F05"
m	%	%
-0.6	16	17
-1.0	16	16

As for the $\widetilde{M_{x1}^*}^{\theta,h}$ signal, it is hard to determine the importance of variations only due to wave from Table 5. To only measure the effects of wave, the amplitude of $\widetilde{F_{x1}^*}^{\theta}$ variations are processed with the same in-house built sinusoidal least mean square method. At -1.0 m, the relative amplitude of this variations is 9 % of mean value and at -0.6 m, it is about 11 %. Even if F_{x1}^* appears to be less sensitive to waves or turbulence than the edgewise moment, wave seems also to contribute to half of the fluctuating load.

4 Conclusion

- While wave doesn't affect Sabella maximum C_P^* at the lower immersion depth -1.0 m, maximum C_P^* decreases from about 10 % at the upper immersion depth -0.6 m.
- Wave increases Magallanes maximum C_P^* of about 10 % at both immersion depth -1.0 m and -0.6 m. Performance is globally lowered at the upper immersion depth, -0.6 m, due to the Reynolds effect seen by Magallanes blades inasmuch as the mean velocity is lower compared to the one at -1.0 m.
- Concerning the Magallanes turbine in the case close to free surface, maximum standard deviation of the edgewise moment is about 100 % of the mean effort when wave is added to turbulence. Fluctuating edgewise moment generated by wave has an amplitude about 46 % of the mean effort at -0.6 m and decreases to the value of 31 % of the mean effort at -1.0 m.
- Concerning the Magallanes turbine in the case close to free surface, maximum standard deviation of the axial force is about 17 % of the mean effort in the wave and turbulence case. Fluctuating axial force generated by waves has an amplitude close to 10 % of the mean effort for both immersion depth: -0.6 m and -1.0 m.
- All in all, both wave and turbulence generate fluctuating loads of similar order of magnitude. Those fluctuating loads add between each other and both contribute to material fatigue.

5 Acknowledgement

This work is co-financed by the European Regional Development Fund (ERDF) through the Interreg Atlantic Area Programme, via the MONITOR project; and through the Interreg V A France (Channel) England Research and Innovation Programme, via the TIGER project. This work benefits from studies carried out within the framework of H2020 MaRINET2 Round Robin tests and the Interreg 2 Seas MET-CERTIFIED project. This project was partly financially supported by the ERDF, the French government, Ifremer and the region Hauts-de-France in the framework of the project CPER 2015–2020 MARCO.

Références

- [1] Tom Blackmore, Luke E. Myers, and AbuBakr S. Bahaj. Effects of turbulence on tidal turbines: Implications to performance, blade loads, and condition monitoring. *International Journal of Marine Energy*, 14:1 – 26, 2016.
- [2] Iver Brevik and Aas Bjørn. Flume experiment on waves and currents. i. rippled bed. *Coastal Engineering*, 3:149–177, 1979.
- [3] Pascal W. Galloway, Luke E. Myers, and AbuBakr S. Bahaj. Quantifying wave and yaw effects on a scale tidal stream turbine. *Renewable Energy*, 63:297 – 307, 2014.
- [4] Benoît Gaurier, Grégory Germain, and Grégory Pinon. How to correctly measure turbulent upstream flow for marine current turbine performances evaluation? In *Advances in Renewable Energies Offshore: Proceedings of the 3rd International Conference on Renewable Energies Offshore (RENEW 2018), October 8-10, 2018, Lisbon, Portugal. 1st Edition. Carlos Guedes Soares (Ed.). ISBN 978-1-138-58535-5. Modelling tidal currents. pp.23-30 (Taylor & Francis Group) .*, 2019.
- [5] Benoît Gaurier, Clément Carlier, Grégory Germain, Grégory Pinon, and Elie Rivoalen. Three tidal turbines in interaction: An experimental study of turbulence intensity effects on wakes and turbine performance. *Renewable Energy*, 2019.
- [6] Benoît Gaurier, Maria Ikhennicheu, Grégory Germain, and Philippe Druault. Experimental study of bathymetry generated turbulence on tidal turbine behaviour. *Renewable Energy*, 156:1158–1170, 2020.
- [7] Xiaoxian Guo, Jianmin Yang, Zhen Gao, Torgeir Moan, and Haining Lu. The surface wave effects on the performance and the loading of a tidal turbine. *Ocean Engineering*, 156:120 – 134, 2018.
- [8] Jean Jacquelin. Regressions and integral equations, April 2014. Lecture available at <https://scikit-guess.readthedocs.io/en/latest/appendices/reei/translation.html>.
- [9] Furgerot L., Sentchev A., Bailly du Bois P., Lopez G., Morillon M., Poizot E., Méar Y., and Bennis A.-C. One year of measurements in alderney race: preliminary results from database analysis. *Philosophical Transactions of the Royal Society A: Mathematical, Physical and Engineering Sciences*, 378(20190625), 2020.
- [10] James McNaughton, Roberta Sinclair, and B Sellar. Measuring and modelling the power curve of a commercial-scale tidal turbine. In *Proceedings of 11th European Wave and Tidal Energy Conference. Nantes, France, sep 2015*.
- [11] O. Duran Medina, F.G. Schmitt, R. Calif, G. Germain, and B. Gaurier. Correlation between synchronised power and flow measurements, a way to characterize turbulence effects on marine current turbine. In *11th European Wave and Tidal Energy Conference (EWTEC)*, September 2015. Nante, France.
- [12] B. Molin. *Hydrodynamique des structures offshore*. Collection des guides pratiques sur les ouvrages en mer. Editions Technip, 2002.
- [13] Myriam Slama, Grégory Pinon, Charifa El Hadi, Michael Togneri, Benoît Gaurier, Grégory Germain, Jean-Valéry Facq, José Nuño, Pablo Mansilla, Erwann Nicolas, Julie Marcille, and André Pacheco. Turbine design dependency to turbulence: An experimental study of three scaled tidal turbines. *Ocean Engineering*, 234:109035, 2021.

-
- [14] Maxime Thiébaud, Jean-François Filipot, Christophe Maisondieu, Guillaume Damblans, Rui Duarte, Eloi Droniou, Nicolas Chaplain, and Sylvain Guillou. A comprehensive assessment of turbulence at a tidal-stream energy site influenced by wind-generated ocean waves. *Energy*, 191:116550, 2020.
- [15] Michael Togneri, Elaine Buck, Alasdair MacLeod, Erwann Nicolas, José Nuño, Michael O'Connor, André Pacheco, Grégory Pinon, and Ian Masters. Multi-model analysis of tidal turbine reliability. In D. Vicinanza, editor, *Proceedings of the Thirteenth European Wave and Tidal Energy Conference*, Università degli Studi della Campania "Luigi Vanvitelli", Italy, Sep 1–Sep 6 2019. EWTEC. ISSN: 2309-1983.
- [16] Michael Togneri, Matt Lewis, Simon Neill, and Ian Masters. Comparison of ADCP observations and 3D model simulations of turbulence at a tidal energy site. *Renewable Energy*, 114:273 – 282, 2017. Wave and Tidal Resource Characterization.